Spin-orbit coupling and magnetic-field dependence of carrier states in a self-assembled quantum dot

Krzysztof Gawarecki*

Department of Theoretical Physics, Faculty of Fundamental Problems of Technology, Wrocław University of Science and Technology, Wybrzeże Wyspiańskiego 27, 50-370 Wrocław, Poland

(Received 12 December 2017; revised manuscript received 2 May 2018; published 7 June 2018)

In this work, we investigate the influence of spin-orbit coupling on the magnetic-field dependence of carrier states in a self-assembled quantum dot. The electron and hole energy levels are calculated using the 6-, 8- and 14-band $\mathbf{k}\cdot\mathbf{p}$ models. Through a detailed study within these models, we extract the information about the impact of various spin-orbital coupling channels on the hole p shell. We demonstrate that the most important contribution comes from the influence of shear strain. We show that the complicated magnetic-field dependence of the hole p shell resulting from numerical simulations can be very well fitted using a phenomenological model. We compare the electron and hole g-factors calculated within 8- and 14-band $\mathbf{k}\cdot\mathbf{p}$ models and show that these methods give reasonably good agreement.

DOI: 10.1103/PhysRevB.97.235408

I. INTRODUCTION

Spin-related properties of carriers confined in quantum dots (QDs) attract much attention due to their potential application in spintronics [1–3]. In particular, the effect of spin-orbit (SO) coupling in QDs was a subject of extensive studies over recent years [4–9]. The lack of inversion symmetry in the crystal lattice (bulk-inversion asymmetry, BIA) leads to the Dresselhaus SO coupling, while asymmetry related to a nanostructure (or induced via external fields) gives rise to the Rashba SO coupling (structure-inversion asymmetry, SIA) [10]. Furthermore, mixing between heavy-hole (hh) and light-hole (lh) subbands significantly affects the overall SO coupling [11,12]. In the case of nanostructures, also other mechanisms related to abrupt material interfaces play a very important role [13]. In the description of QDs' spectra, some theoretical works [4,8,9] utilize the effective Fock-Darwin model supplemented by additional terms (described by empirical parameters), which are referred to the Rashba or/and Dresselhaus SO coupling. Such a model qualitatively describes basic QD properties and (if taken with realistic parameters) can predict correct spin ordering of the several lowest single-particle states.

The spin dynamics of a QD system can be driven by applying an external magnetic field. However, the response of the system strongly depends on the parameters, which cannot be simply deduced from the bulk values. In consequence, spin control needs a precise knowledge of the carrier states in the system, which requires advanced modeling. One of the important issues is related to the electron/hole g factor, which in the case of QD can differ by an order of magnitude from the bulk value [14]. The g factor in a QD was investigated in many experimental works [7,15–22] and theoretical studies including tight-binding [23,24] and $\mathbf{k}\cdot\mathbf{p}$ [19–22] modeling. The magnetic-field dependence of the hole energy levels were investigated within 4-band $\mathbf{k}\cdot\mathbf{p}$ [25], where, while lh-hh subband mixing was included, the influence of various SO mechanisms and anisotropy, were neglected. Also in Ref. [6], the hole states in presence of magnetic field were studied. In that work, the subband mixing enters via Luttinger Hamiltonian, and the Rashba coupling is accounted for by a free parameter.

In this paper, we study the magnetic-field dependence of the electron and hole states. We show that quantitative and qualitative reconstruction of the hole p-shell energy levels results from the interplay of several SO mechanisms with the most important contribution from the one that depends on the shear strain. We utilize the 14-band $\mathbf{k}\cdot\mathbf{p}$ model, which inherently accounts for the Rashba, Dresselhaus, and other spin-orbit coupling mechanisms. We show that the results from the 14-band $\mathbf{k}\cdot\mathbf{p}$ theory can be very well fitted via an extended Fock-Darwin model with the structural asymmetry and SO interaction taken into account. Finally, we calculate the electron and hole g factors using 8- and 14-band $\mathbf{k}\cdot\mathbf{p}$ models and show that these methods give reasonably good agreement.

The paper is organized as follows. In Sec. II, we briefly describe the models that are used to calculate the strain distribution and the carrier states. In Sec. III, we present and discuss the results of numerical simulations. Section IV contains concluding remarks. Finally, a detailed description of the model is given in the Appendix.

II. MODEL

The system under consideration contains a single self-assembled QD formed by InGaAs in GaAs matrix. The dot is lens shaped with the diameter of 24 nm, the height of 4.2 nm, and is placed on a 0.6-nm-thick wetting layer (WL). We consider the uniform [Fig. 1(a)] and with simulated material intermixing [Fig. 1(b)] $In_xGa_{1-x}As$ distribution. In the latter case, the material distribution is processed by Gaussian blur with a standard deviation of 1.2 nm. The inhomogeneous composition is described by the function $C(\boldsymbol{r})$, where $C(\boldsymbol{r}) = 1$ refers to pure InAs, $C(\boldsymbol{r}) = 0$ to pure GaAs, and intermediate

*Krzysztof.Gawarecki@pwr.edu.pl

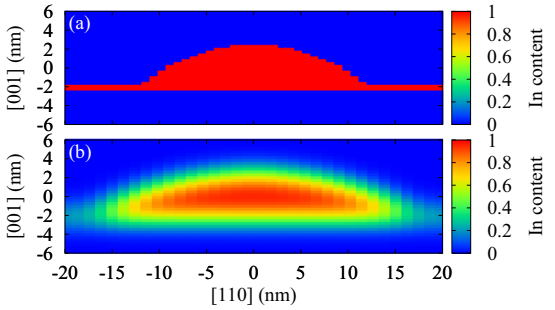

FIG. 1. Material distribution in the system, in the case of uniform (a) and blurred (b) QD.

values correspond to $In_xGa_{1-x}As$. The spectral properties of the system are affected by strain, which is caused by an InAs/GaAs lattice mismatch. The strain distribution is modeled within the continuous elasticity approach [26]. The piezoelectric potential $V(\boldsymbol{r})$ is calculated by solving the equation $\rho(\boldsymbol{r}) = \varepsilon_0 \nabla[\varepsilon_r(\boldsymbol{r})\nabla V(\boldsymbol{r})]$, where $\varepsilon_r(\boldsymbol{r})$ is the position-dependent relative permittivity. The charge density is calculated from $\rho(\boldsymbol{r}) = -\nabla \cdot \boldsymbol{P}(\boldsymbol{r})$, where the piezoelectric polarization is accounted for up to the second order with respect to the strain-tensor elements [27] with parameters taken from Ref. [28].

In order to calculate the electron and hole states, we implemented the 14-band $\mathbf{k}\cdot\mathbf{p}$ model. In this framework, (in contrast to 8- and fewer-band approaches) the kinetic part of the Hamiltonian correctly describes the symmetry (C_{2v}) of the zinc-blende crystal [29]. Furthermore, the model inherently contains the Dresselhaus, Rashba, and other coupling mechanisms, which, in the fewer-band models, need to be represented via additional perturbative terms [10]. The Hamiltonian of the system can be written as $H = H^{(\mathrm{k})} + H^{(\mathrm{str})} + H^{(\mathrm{m})} + V$, where $H^{(\mathrm{k})}$ is the kinetic part of the Hamiltonian, $H^{(\mathrm{str})}$ accounts for the strain, and $H^{(\mathrm{m})}$ represents the magnetic interaction. The Hamiltonian can be divided into blocks according to the symmetry classification [10,30]. In the case of the extended Kane model (14 bands), Γ_{8c}, Γ_{7c} Γ_{6c}, Γ_{8v}, and Γ_{7v} bands are taken into account explicitly and the remote band contribution enters via material parameters [10,30]. We keep the Burt-Foreman operator ordering [31] in its extended version proposed in Ref. [32]. The magnetic field is introduced via Peierls substitution within the gauge-invariant scheme, described in detail in Ref. [33]. The electron and hole states are obtained by diagonalizing the Hamiltonian. The in-plane probability density of the nth electron/hole state is calculated using the formula

$$d_n^{(\mathrm{e/h})}(x,y) = \sum_{m=1}^{14} \int_{-\infty}^{\infty} \psi_{n,m}^{(\mathrm{e/h})*}(\boldsymbol{r}) \psi_{n,m}^{(\mathrm{e/h})}(\boldsymbol{r}) dz,$$

where $\psi_{n,m}^{(\mathrm{e/h})}(\boldsymbol{r})$ denotes the mth-band component of the nth electron/hole wave function. The average values of the z components of the electron and hole envelope angular momenta read as

$$\langle M_z \rangle = \sum_{m=1}^{14} \int_{-\infty}^{\infty} \psi_{n,m}^{(\mathrm{e/h})*}(\boldsymbol{r}) \left(iy \frac{\partial}{\partial x} - ix \frac{\partial}{\partial y} \right) \psi_{n,m}^{(\mathrm{e/h})}(\boldsymbol{r}) d\boldsymbol{r}.$$

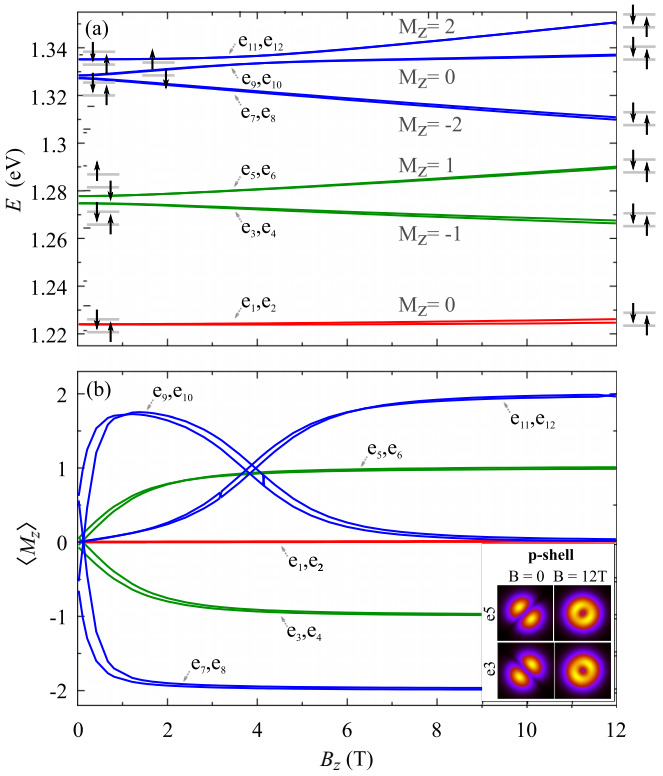

FIG. 2. (a) Magnetic-field dependence of the 12 lowest electron states in the uniform InAs QD. Energy $E = 0$ refers to the unstrained GaAs valence band edge. Schematic pictures on the left describe spin configuration at magnetic field close to zero, while insets on the right present the configuration at $B = 12$ T. (b) Corresponding axial projection of the envelope angular momentum. The inset in the right bottom corner presents the in-plane probability density of e_3 and e_5 states at $B_z = 0$ and $B_z = 12$ T.

A full description of the Hamiltonian and calculation details are given in the Appendix.

III. RESULTS

This section presents the results for the magnetic-field dependence of the lowest-energy electron and hole states. The eigenstates are 14-element pseudospinors, where each part refers to one of the bands: Γ_{8c}, Γ_{7c} Γ_{6c}, Γ_{8v}, or Γ_{7v}. Since the considered QD has a geometrical axial symmetry, the states are labeled according to the axial components of their approximate *envelope* angular momenta (s, p, d shells).

A. Electron states

The electron energy levels in the uniform InAs QD as a function of external axial magnetic field are shown in Fig. 2(a). The corresponding average values of the axial projection of the envelope angular momentum $\langle M_z \rangle$ are presented in Fig. 2(b). The two lowest-energy states (e_1,e_2) are s type with $\langle M_z \rangle \approx 0$. Their energies increase according to the diamagnetic shift $\alpha_s^{(\mathrm{e})} B_z^2$, where fitting to the numerical results gives $\alpha_s^{(\mathrm{e})} = 10.04\ \mu\mathrm{eV/T}^2$. The energy splitting between the two lowest s-type states can be attributed to the effective Landé factor $g_\mathrm{e} = (E_{s\uparrow} - E_{s\downarrow})/\mu_B B_z = -2.17$. This value differs significantly

from the electron bulk g factor, averaged according to the local composition

$$\langle g\rangle = \sum_{m=1}^{14}\int_{-\infty}^{\infty}\psi^{(e)*}_{s,m}(\boldsymbol{r})g(\boldsymbol{r})\psi^{(e)}_{s,m}(\boldsymbol{r})d\boldsymbol{r} = -13.17,$$

where $g(\boldsymbol{r}) = C(\boldsymbol{r})g_{\mathrm{InAs}} + [1 - C(\boldsymbol{r})]g_{\mathrm{GaAs}}$, with $g_{\mathrm{InAs}} = -14.9$ and $g_{\mathrm{GaAs}} = -0.44$. This discrepancy is caused by the renormalization of the effective gap and the angular momentum quenching [14]. In fact, the Landé factor g_e tends to the bulk value in the limit of a very large dot and to $g_0 = 2$ in the limit of a very small dot with strong confinement [14]. The next four states [$e_3 - e_6$, green lines in Fig. 2(a)] exhibit the p-type symmetry. The splitting at $B = 0$ is caused by the piezoelectric field and (with smaller contribution) by the spin-orbit coupling. These pairs of states exhibit large Zeeman splitting due to their nonzero envelope angular momenta. As shown in the inset of Fig. 2(b), in weak magnetic field the p-type states are oriented along [110] and [1$\bar{1}$0] axes. In consequence, their $\langle M_z\rangle$ is close to zero. However, the magnetic field leads to the mixing of these states and tends to form of $|p_{\pm1}\rangle \propto (|p_{110}\rangle \pm i|p_{1\bar{1}0}\rangle)$ with $M_z = \pm1$, which are clearly visible at $B_z > 4$ T. Finally, the last three pairs of states belong to the d shell [e_7–e_{12}, plotted with blue lines in Fig. 2(a)], for sufficiently strong magnetic field they form $M_z \approx -2,0,2$ configurations. At about $B = 4$ T there is an anticrossing between the states with $M_z \approx 0$ and $M_z \approx 2$. All of the considered electron states are mainly Γ_{6c} with very small admixtures from the other groups of bands. In consequence, their axial projection of the *band* angular momentum $j_z^{(e)}$ is approximately $\pm\frac{1}{2}$.

Although the structure of the electron energy levels resembles the one that results from the standard Fock-Darwin model, the obtained spin configuration is more complicated. The reason is the spin-orbit coupling, which affects the spin and spectral properties of a QD [4]. The total spin-orbit coupling favors the configurations where the electron spin and envelope angular momentum are antiparallel. In consequence, for positive M_z and weak magnetic fields, the spin configuration is inverted compared to the s-shell states [left spin diagrams in Fig. 2(a)]. However, at stronger magnetic fields, the energy related to the Zeeman term dominates and the spin configuration returns to the "usual" case where the lower-energy state has spin oriented up [spin diagrams on the right in Fig. 2(a)]. This situation takes place for e_5, e_6 pair of states ($M_z \approx 1$): at about $B_z = 1.61$ T there is a crossing between these states, in the case of e_{11}, e_{12} ($M_z \approx 2$) states, this occurs for 11.7 T.

The complicated magnetic-field dependence of the p shell can be interpreted within a phenomenological model involving five parameters. This corresponds to the Fock-Darwin model with a spin-orbit term included [4]. The relevant Hamiltonian is

$$\begin{aligned} H_p^{\mathrm{eff}} &= V_{\mathrm{a}}(|+1\rangle\langle -1| + \mathrm{H.c.}) \otimes \mathbb{1} + \frac{1}{2\hbar}V_{\mathrm{SO}}L_z \otimes \sigma_z \\ &+ \frac{1}{2}\mu_B g_p B_z \mathbb{1} \otimes \sigma_z + \frac{1}{\hbar}W B_z L_z \otimes \mathbb{1} \\ &+ \alpha_p B_z^2 \mathbb{1} \otimes \mathbb{1}, \end{aligned} \tag{1}$$

TABLE I. The effective parameters describing the electron p shell obtained from the fitting procedure. The superscript (e) refers to the electron.

	Uniform QD	Blurred QD
$V_{\mathrm{a}}^{(e)}$ (meV)	1.513	0.651
$V_{\mathrm{SO}}^{(e)}$ (meV)	0.173	0.370
$g_p^{(e)}$	−1.353	−0.695
$W^{(e)}$(meV/T)	0.949	0.900
$\alpha_p^{(e)}(\mu\mathrm{eV/T}^2)$	14.76	13.20

where the tensor product is related to the formal subsystems of the envelope and the band angular momentum, $|\pm 1\rangle$ refers to M_z, V_{a} is a parameter that accounts for the system anisotropy, $\mathbb{1}$ is the unit operator, σ_z is the axial Pauli matrix, L_z is the operator of the axial projection of the envelope angular momentum, g_p is the effective g factor for the p shell, and W is a parameter related to the influence of the envelope angular momentum. In the basis $\{|+1\uparrow\rangle, |-1\uparrow\rangle, |+1\downarrow\rangle, |-1\downarrow\rangle\}$ (where the number refers to M_z and the arrow to the spin orientation with respect to the z axis) the Hamiltonian can be written in a form of a 4×4 matrix

$$\begin{aligned} H_p^{\mathrm{eff}} = V_{\mathrm{a}}&\begin{pmatrix}0&1&0&0\\1&0&0&0\\0&0&0&1\\0&0&1&0\end{pmatrix} + V_{\mathrm{SO}}\begin{pmatrix}\frac{1}{2}&0&0&0\\0&-\frac{1}{2}&0&0\\0&0&-\frac{1}{2}&0\\0&0&0&\frac{1}{2}\end{pmatrix} \\ &+ WB_z\begin{pmatrix}1&0&0&0\\0&-1&0&0\\0&0&1&0\\0&0&0&-1\end{pmatrix} + \alpha_p B_z^2\begin{pmatrix}1&0&0&0\\0&1&0&0\\0&0&1&0\\0&0&0&1\end{pmatrix} \\ &+ \mu_B g_p B_z\begin{pmatrix}\frac{1}{2}&0&0&0\\0&\frac{1}{2}&0&0\\0&0&-\frac{1}{2}&0\\0&0&0&-\frac{1}{2}\end{pmatrix}. \end{aligned}$$

We fitted the phenomenological parameters to the electron p shell (Table I) and obtained an excellent agreement to the 14 $\mathbf{k}\cdot\mathbf{p}$ numerical results (see Fig. 3). The blurred QD gives larger spin-obit term, but smaller anisotropy compared to the

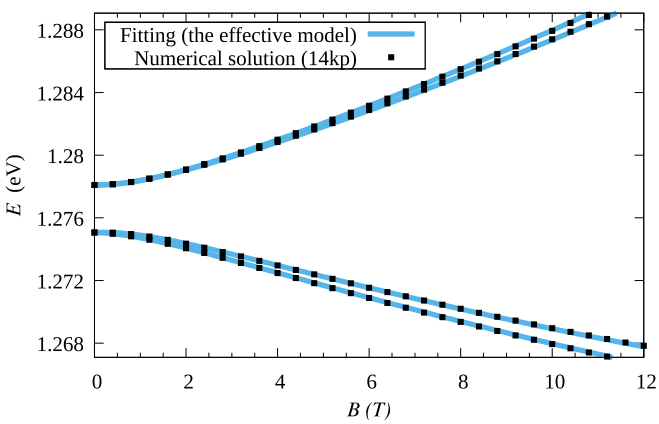

FIG. 3. Magnetic-field dependence of the electron p-shell energy levels in the uniform InAs QD.

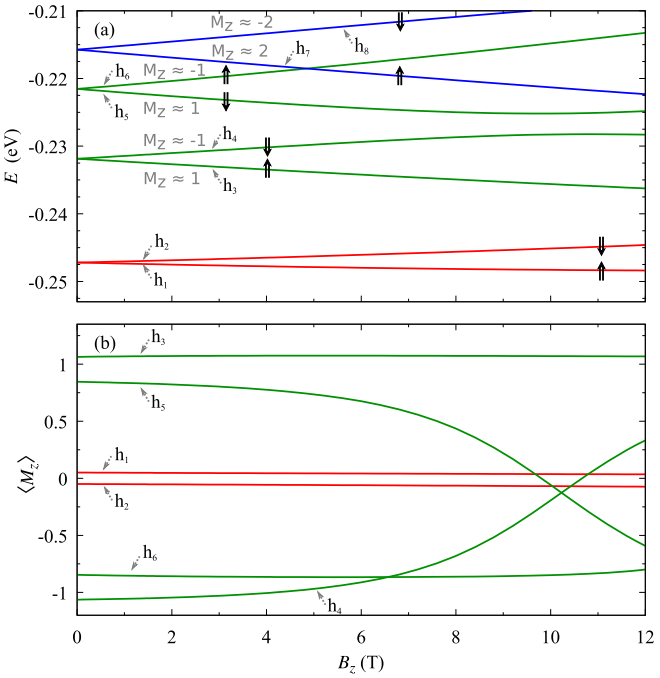

FIG. 4. (a) Magnetic-field dependence of the lowest hole energy levels. Energy $E = 0$ refers to the unstrained GaAs valence band edge. (b) Corresponding axial projection of the envelope angular momentum.

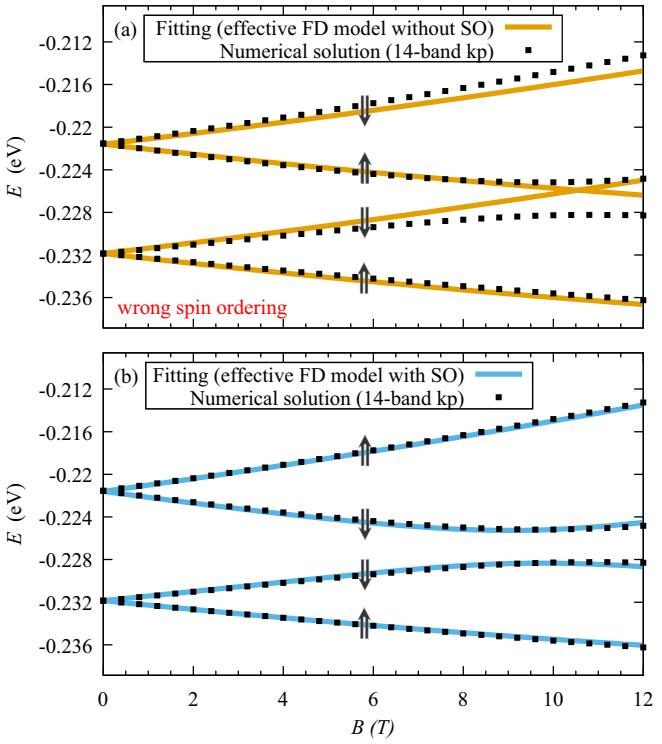

FIG. 5. Magnetic-field dependence of the hole p-shell energy levels in the uniform InAs QD. Solid lines denote the results obtained from the effective model for a fitting (a) without SO parameter, (b) with SO parameter included.

uniform QD. Since $V_{\mathrm{SO}}^{(\mathrm{e})}$ is relatively small for both of the dots, it is possible to obtain a reasonably good fit also for the standard Fock-Darwin model (which corresponds to $V_{\mathrm{SO}}^{(\mathrm{e})} = 0$). However, at low magnetic fields, this produces a wrong spin ordering of some states (in the case of the p shell, wrong spin ordering appears at $B_z < 1.61$ T for the uniform QD, and $B_z < 10.7$ T for the blurred QD). The overall spin-orbit coupling in the p shell ($V_{\mathrm{SO}}^{(\mathrm{e})}$) is caused by the interplay of the abrupt material interfaces, the Rashba coupling, shear strain in H_{6c8v} and H_{6c7v}, the Dresselhaus coupling, and the subband mixing.

B. Hole states

The valence band states (directly resulting from the numerical simulations) are converted to the hole states by the operation of time reversal, which inverts the envelope and band angular momenta. The energy scale is reversed. The magnetic-field dependence of the lowest-energy hole levels (s, p and the two lowest states from the d shell) is shown in Fig. 4(a) and the corresponding axial projections of the envelope angular momenta are given in Fig. 4(b). Due to a complicated pattern of the higher states, the angular momenta are shown up to the p shell. Contrary to the electron case, the alignment of hole energy levels does not exhibit a clear shell structure [34–37]. The energy splitting between the two lowest-energy states (s type, $M_z \approx 0$) is significantly larger than in the electron case. The relevant effective g factor is $g_{\mathrm{h}} = (E_{s\Uparrow} - E_{s\Downarrow})/\mu_B B_z = -5.51$. Note that with this sign convention, the exciton g factor is given by $g_X = [E_X(\sigma_+) - E_X(\sigma_-)]/\mu_B B_z = -g_{\mathrm{e}} + g_{\mathrm{h}}$, where the energies $E_X(\sigma_\pm)$ are related to the absorption of the circularly polarized ($\sigma_\pm$) light [32]. The fitting yielded diamagnetic parameter of $\alpha_s^{(\mathrm{h})} = 4.955\ \mu\mathrm{eV/T}^2$.

The next four states belong to the p shell. Large splitting between their spin doublets at $B = 0$ arises from a combination of the spin-orbit coupling and the influence of the piezoelectric potential. Unlike the electron states, even at low magnetic field the $M_z \approx \pm 1$ configurations are well defined. At about $B = 10.2$ T, there is an anticrossing, which involves the same spin orientation but different envelope angular momenta. Finally, at about $B = 4.8$ T there is a crossing between $M_z \approx -1$ state and the one from the d shell (with $M_z \approx 2$). The considered p-type states are mostly heavy holes with relatively small (below 10%) admixture from the other subbands, so their total axial projections of the band angular momenta can be approximated by $j_z^{(\mathrm{h})} \approx \pm\frac{3}{2}$.

Similarly to the electron case, the magnetic-field dependence of the p-type states can be described using the effective model. We fitted the parameters of Eq. (1) to the hole p shell. Figure 5 presents 14-band $\mathbf{k}\cdot\mathbf{p}$ results of the energy branches compared to the effective model in two cases: (a) the fitting without the SO term ($V_{\mathrm{SO}}^{(\mathrm{h})} = 0$) and (b) with SO included. The first case corresponds to the pure Fock-Darwin model, for which the results are not only inaccurate from the quantitative point of view, but also predict a wrong spin ordering. In particular, this leads to the lack of the pronounced anticrossing at $B_z = 10.2$ T. On the other hand, the full effective model [Fig. 5(b)] gives correct spin ordering and a very good agreement with the numerical 14-band $\mathbf{k}\cdot\mathbf{p}$ results. The width of the pronounced avoided crossing at $B = 10.2$ T

TABLE II. The effective parameters for hole p shell obtained from a fitting procedure, (*) denotes a fitting without the SO parameter. The superscript (h) refers to the hole.

	Uniform QD*	Uniform QD	Blurred QD
$V_a^{(h)}$ (meV)	5.13	1.54	0.495
$V_{SO}^{(h)}$ (meV)	0.0	−9.79	−7.31
$g_p^{(h)}$	−16.80	2.62	2.14
$W^{(h)}$(meV/T)	0.0	−0.523	−0.425
$\alpha_p^{(h)}(\mu eV/T^2)$	7.28	7.28	3.83

depends on the anisotropy. In the considered system, a large contribution to it comes from the piezoelectric potential. The anisotropy parameter can be extracted from the energy levels by $V_a^{(h)} = [E_{h5}(10.2\ T) - E_{h4}(10.2\ T)]/2$. Then, the SO term is calculated from $V_{SO}^{(h)} = -\sqrt{[E_{h5}(0) - E_{h4}(0)]^2 - 4(V_a^{(h)})^2}$. The other parameters are derived from the fitting procedure, and all of them are listed in Table II. In contrast to the electron case, both anisotropy ($V_a^{(h)}$) and spin-orbit parameter ($V_{SO}^{(h)}$) are larger in the case of the uniform QD. Hence, $g_p^{(h)}$ and $W^{(h)}$ differ in their sign, the splitting of h_5–h_6 is larger than h_3–h_4. This is consistent with the experimental results [7,38], where the splitting between upper lines in the p shell is larger compared to the lower doublet. On the other hand, the p-shell anticrossing (h_4–h_5) is not clearly visible in the available experiments [7,38]. This could be caused by the Coulomb interaction. In the case of the neutral exciton in a single QD [7], the Coulomb interaction mixes the exciton states with the same total envelope angular momenta ($M_{exc} = M_e + M_h$). In consequence, the configuration ($M_e = \pm 1$, $M_h = \mp 1$) is coupled to ($M_e = \mp 1$, $M_h = \pm 1$), and this leads to qualitative spectrum reconstruction. On the other hand, in the C-V measurements with hole charging [38], the Coulomb interaction between holes also could play important role because it reduces an anisotropy. In fact, it has been shown that the Coulomb interaction leads to the reduction of the p-shell anticrossing [6]. In order to reduce Coulomb effects, the magnetic-field dependence of the single-hole energy levels can be measured in experiments based on double quantum dots [39]. In such a case, the single-particle energy levels are determined from the spectrum of the indirect exciton, where the Coulomb interaction is much weaker compared to the direct one [39].

The spin-orbit-induced reconstruction of the spectrum leads to considerable mixing of spin states. This can be expected to modify selection rules, both for p-shell optical transitions and for tunnel coupling to a neighboring dot. It should also induce strong admixture mechanisms in a double-QD structure, resulting in accelerated spin relaxation. Identification of the most pronounced spin-orbit coupling mechanism for a given system gives a possibility to control this effect by a proper growth of the sample. For example, the abrupt material interfaces could be softened by annealing, shear strain could be reduced by using a strain-reducing layer, and the strength of the Dresselhaus coupling could be (partially) controlled by the material composition. In order to assess various contributions to the overall spin-orbit coupling in the p shell, we performed fitting to the results of calculation within several degrees of approximation:

TABLE III. The effective spin-orbit parameter $V_{SO}^{(h)}$ for hole p shell obtained from various approximations. All of the parameter definitions are given in the Appendix.

		Value of $V_{SO}^{(h)}$ (meV)	
No.	Model	Uniform QD	Blurred QD
1.	14 $\mathbf{k}\cdot\mathbf{p}$ full	−9.848	−7.312
2.	8 $\mathbf{k}\cdot\mathbf{p}$ full	−9.916	−7.379
3.	8 $\mathbf{k}\cdot\mathbf{p}$, neglected $d_v = 0$	−3.460	−1.558
4.	8 $\mathbf{k}\cdot\mathbf{p}$, neglected $d_v = 0$, $C_k = 0$ and Dresselhaus terms $H^D = 0$	−3.446	−1.532
5.	6 $\mathbf{k}\cdot\mathbf{p}$ full	−10.512	−8.120
6.	6 $\mathbf{k}\cdot\mathbf{p}$, neglected $H^{(m)} = 0$ and $\gamma_3 = 0$, $d_v = 0$	0.0	0.0

(1) The full 14-band $\mathbf{k}\cdot\mathbf{p}$ model. All of the terms in the Hamiltonian are present.

(2) The full 8-band $\mathbf{k}\cdot\mathbf{p}$ model. The Dresselhaus SO coupling (which arises from the coupling to Γ_{8c} and Γ_{7c}) is accounted for via perturbative terms (see $H^{(D)}$ in the Appendix). The model inherently contains also the Rashba coupling (except some relatively small contributions from the coupling to Γ_{8c} and Γ_{7c}) and other spin-orbit mechanisms related to the material inhomogeneity at the interfaces.

(3) The same as (2), but with $d_v = 0$ hence with the influence of the shear strain in the valence band neglected.

(4) The same as (3), with further reduction of spin-orbit coupling by disabling the Dresselhaus terms ($H^D = 0$) and neglecting small contribution from C_k (k-linear terms).

(5) This approximation is based on the 6-band $\mathbf{k}\cdot\mathbf{p}$ model (valence bands only). The deformation potential d_v is present. The Dresselhaus coupling is neglected and $C_k = 0$. The model partially accounts for the Rashba coupling via position dependence of the κ and q parameters in the magnetic Hamiltonian ($H^{(m)}$ in the Appendix). However, this contribution is overestimated due to the lack of some terms with the opposite sign.

(6) The same as (5), but without the magnetic part of the Hamiltonian ($H^{(m)}$), influence of the shear strain is neglected, $d_v = 0$. The contribution from subband mixing [13] is removed by setting $\gamma_3 = 0$.

As shown in Table III, for both types of QDs the most important contribution to $V_{SO}^{(h)}$ comes from the shear strain, which enters to the valence band block of the Hamiltonian with the deformation potential d_v. The impact of the Dresselhaus terms is small. Furthermore, the results from 8- and 14-band $\mathbf{k}\cdot\mathbf{p}$ are in very good agreement. On the other hand, 6-band $\mathbf{k}\cdot\mathbf{p}$ overestimates the p-shell spin-orbit coupling. The piezoelectric field is very important for anisotropy ($V_a^{(h)}$) but its contribution to $V_{SO}^{(h)}$ is negligible.

We calculated also electron and hole g factors and compared the accuracy of various multiband approaches. Figures 6(a) and 6(b) show electron g factor as a function of the dot composition. In the absolute values, there is a good agreement between 8- and 14-band $\mathbf{k}\cdot\mathbf{p}$, the relative discrepancy between them increases with decreasing InAs content (as the g factor decreases). The comparison 8-band $\mathbf{k}\cdot\mathbf{p}$ to 2-band $\mathbf{k}\cdot\mathbf{p}$ is widely discussed in Ref. [40]. Figures 6(c) and

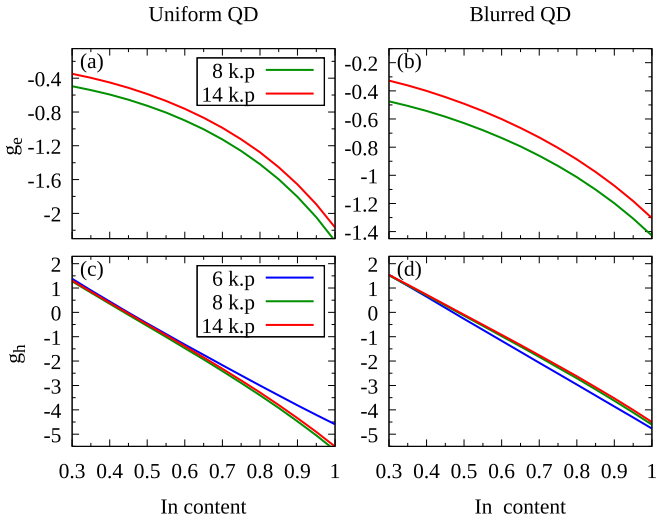

FIG. 6. The electron (a), (b) and hole (c), (d) g factor as a function of material composition in the case of uniform and blurred QD.

6(d) show the hole g factor obtained from 6-, 8-, and 14-band $\mathbf{k}\cdot\mathbf{p}$ models. Due to the ellipticity condition in the 14-band $\mathbf{k}\cdot\mathbf{p}$, we reduced the optical matrix parameter $Q \to Q_r = 0.8Q$ (see the Appendix). As Q contributes to the g factors in the second power, the discrepancy between 8- and 14-band models could be larger by up to 36% as compared to the present values. For both the electron and hole, the values of g factors for the blurred QD are significantly reduced, which can be related to the enhanced GaAs content in the dot.

IV. CONCLUSIONS

We have calculated the magnetic-field dependence of the electron and hole states in a QD. We have investigated the influence of the spin-orbit coupling on the structure of electron and hole states. The results show that the dominant contribution to the overall spin-orbit coupling in the hole p shell comes from the shear strain, while the impact of Dresselhaus terms is small. We have shown that numerical results can be very well reproduced by an empirical Fock-Darwin model, if a term representing spin-orbit coupling is included. Finally, we have compared the values of electron and hole g factors obtained from 8- and 14-band $\mathbf{k}\cdot\mathbf{p}$ models and have shown that these methods are in a reasonably good agreement.

ACKNOWLEDGMENTS

This work was supported by the Polish National Science Centre (Grant No. 2014/13/B/ST3/04603). Calculations have been carried out in Wroclaw Centre for Networking and Supercomputing (http://www.wcss.wroc.pl), Grant No. 203. I would like to thank P. Machnikowski and M. Zieliński for their helpful suggestions. I am also grateful to M. Gawełczyk for valuable comments and sharing his implementation of the blur algorithm.

APPENDIX: CALCULATION DETAILS

The kinetic part of the Hamiltonian can be expressed in terms of the invariants [10]

$$
\begin{aligned}
H^{(k)}_{8c8c} &= E'_g + \Delta'_0,\\
H^{(k)}_{7c7c} &= E'_g,\\
H^{(k)}_{6c6c} &= E_g + k_x \frac{\hbar^2}{2m'} k_x + \text{c.p.},\\
H^{(k)}_{8v8v} &= -\frac{\hbar^2}{2m_0}\Big\{k_x\gamma'_1 k_x - 2\Big(J_x^2 - \frac{1}{3}J^2\Big)k_x\gamma'_2 k_x\\
&\quad -2\gamma'_3\{J_x,J_y\}(k_x\gamma'_3 k_y + k_y\gamma'_3 k_x) + \text{c.p.}\Big\}\\
&\quad +\frac{1}{\sqrt{3}}\big[\{J_x, J_y^2 - J_z^2\}(C_k k_x + k_x C_k) + \text{c.p.}\big],\\
H^{(k)}_{7v7v} &= -\Delta_0 - \frac{\hbar^2}{2m_0} k_x\gamma'_1 k_x,\\
H^{(k)}_{8c7c} &= 0,\\
H^{(k)}_{8c6c} &= -\sqrt{3}P'(U_x k_x + \text{c.p.}),\\
H^{(k)}_{8c8v} &= -\tfrac{2}{3}Q_r(\{J_y,J_z\}k_x + \text{c.p.}) + \tfrac{1}{3}\Delta^-,\\
H^{(k)}_{8c7v} &= -2Q_r(U_{yz}k_x + \text{c.p.}),\\
H^{(k)}_{7c6c} &= \frac{1}{\sqrt{3}}P'(\sigma_x k_x + \text{c.p.}),\\
H^{(k)}_{7c8v} &= -2Q_r(T_{yz}k_x + \text{c.p.}),\\
H^{(k)}_{7c7v} &= -\tfrac{2}{3}\Delta^-,\\
H^{(k)}_{6c8v} &= \sqrt{3}(T_x k_x + \text{c.p.})P,\\
H^{(k)}_{6c7v} &= -\frac{1}{\sqrt{3}}(\sigma_x k_x + \text{c.p.})P,\\
H^{(k)}_{8v7v} &= -\frac{\hbar^2}{2m_0}[-6U_{xx}k_x\gamma'_2 k_x\\
&\quad -6U_{xy}(k_x\gamma'_3 k_y + k_y\gamma'_3 k_x) + \text{c.p.}]\\
&\quad -i\frac{\sqrt{3}}{2}[U_{yz}(C_k k_x + k_x C_k) + \text{c.p.}],
\end{aligned}
$$

where c.p. denotes the cyclic permutation of indices; $\{A,B\} = (AB + BA)/2$, E_g, E'_g are the energy gaps between Γ_{8v}–Γ_{6c} and Γ_{8v}–Γ_{7c}, respectively, $\Delta_0, \Delta'_0, \Delta^-$ are parameters related to the spin-orbit coupling, P, P', Q_r are proportional to the interband momentum matrix elements, m_0 is the free-electron mass, m' and γ'_i are modified values of the effective mass and Luttinger parameters. The relations between the modified and the original parameters (listed in Table IV) are given further. The matrices σ_i are the Pauli matrices, J_i are the matrices of angular momentum $j = 3/2$, U_i, U_{ij} are Hermitian conjugates of T_i, T_{ij}, respectively (definitions are given in given in Refs. [10,30,32]). k_i is represented as a spatial derivative in the real space. Then, a discretization is performed using the finite-difference method [41]. We avoid spurious solution problem related to the first-order derivatives [42] by applying the central four-point scheme.

TABLE IV. Material parameters used in the calculations [10,43].

	GaAs	InAs	Bowing
m_e^*	$0.0665m_0$	$0.0229m_0$	$0.0091m_0$
E_v	0.0 eV	0.21 eV	
E_g	1.519 eV	0.417 eV	0.477 eV
E_g'	4.488 eV	4.390 eV	
P	Calculated from $P=\sqrt{E_P\hbar^2/(2m_0)}$		
P'	$4.78i$ eV Å	$0.873i$ eV Å	
Q	8.165 eV Å	8.331 eV Å	
Q_r	Reduced value $Q_r=0.8Q$		
γ_1	6.98	20.0	
γ_2	2.06	8.5	
γ_3	2.93	9.2	
C_k	−0.0034 eV Å	−0.0112 eV Å	
Δ_0	0.341 eV	0.39 eV	0.15 eV
Δ_0'	0.171 eV	0.24 eV	
Δ'	-0.05i eV	0.0	
a_c	−7.17 eV	−5.08 eV	2.61 eV
a_v	1.16 eV	1.00 eV	
b_v	−2.0 eV	−1.8 eV	
d_v	−4.8 eV	−3.6 eV	
g	−0.44	−14.9	
κ	1.2	7.6	
q	Calculated from $q=\frac{2m_0}{\hbar^2}\frac{2}{9}\left(\frac{Q^2}{E_g}-\frac{Q^2}{E_g+\Delta_0'}\right)$		

Strain enters into the Hamiltonian via terms [10]

$$H^{(\mathrm{str})}_{6c6c}=a_c\mathrm{Tr}\,[\epsilon],$$

$$H^{(\mathrm{str})}_{8v8v}=a_v\mathrm{Tr}\,[\epsilon]-b_v\left[\left(J_x^2-\frac{1}{3}J^2\right)\epsilon_{xx}+\mathrm{c.p.}\right]-\frac{d_v}{\sqrt{3}}\left[2\{J_x,J_y\}\epsilon_{xy}+\mathrm{c.p.}\right],$$

$$H^{(\mathrm{str})}_{7v7v}=a_v\mathrm{Tr}\,[\epsilon],$$

$$H^{(\mathrm{str})}_{6c8v}=-2\sqrt{3}\left(T_x\sum_{j=x,y,z}k_j\epsilon_{xj}+\mathrm{c.p.}\right)P,$$

$$H^{(\mathrm{str})}_{6c7v}=\frac{2}{\sqrt{3}}\left(\sigma_x\sum_{j=x,y,z}k_j\epsilon_{xj}+\mathrm{c.p.}\right)P,$$

$$H^{(\mathrm{str})}_{8v7v}=-3b_v(U_{xx}\epsilon_{xx}+\mathrm{c.p.})-\sqrt{3}d_v(2U_{xy}\epsilon_{xy}+\mathrm{c.p.}),$$

where a_c, a_v, b_v, d_v are deformation potentials. Magnetic interaction is accounted for via the following terms [32]:

$$H^{(\mathrm{m})}_{8c8c}=\frac{g_0}{3}\mu_B\boldsymbol{J}\cdot\boldsymbol{B},$$

$$H^{(\mathrm{m})}_{8c7c}=-g_0\mu_B\boldsymbol{U}\cdot\boldsymbol{B},$$

$$H^{(\mathrm{m})}_{7c7c}=-\frac{g_0}{6}\mu_B\boldsymbol{\sigma}\cdot\boldsymbol{B},$$

$$H^{(\mathrm{m})}_{6c6c}=i\frac{\hbar^2}{4m_0}[(k_xg'k_y-k_yg'k_x)\sigma_z+\mathrm{c.p.}],$$

$$H^{(\mathrm{m})}_{8v8v}=-i\frac{\hbar^2}{m_0}[(k_x\kappa'k_y-k_y\kappa'k_x)J_z+\mathrm{c.p.}]-i\frac{\hbar^2}{m_0}\left[(k_xq'k_y-k_yq'k_x)J_z^3+\mathrm{c.p.}\right],$$

$$H^{(\mathrm{m})}_{7v7v}=-i\frac{\hbar^2}{m_0}[(k_x\kappa'k_y-k_y\kappa'k_x)\sigma_z+\mathrm{c.p.}]-\mu_B\boldsymbol{\sigma}\cdot\boldsymbol{B},$$

$$H^{(\mathrm{m})}_{8v7v}=-i\frac{3\hbar^2}{2m_0}[(k_x\kappa'k_y-k_y\kappa'k_x)U_z+\mathrm{c.p.}]-3\mu_B\boldsymbol{U}\cdot\boldsymbol{B},$$

where $g_0=2$, g', κ', and q' are related to the electron and hole g factors. In the case of a nanostructure, the above elements are nonzero even at $B=0$ and κ' introduces the Burt-Foreman operator ordering, which represents boundary conditions at the interface [31,44]. In the presence of magnetic field $k_nk_m-k_mk_n=-i\varepsilon_{nmk}eB_k/\hbar$, where ε_{nmk} denotes the Levi-Civita symbol. For the calculation in 14-band $\mathbf{k}\cdot\mathbf{p}$, the contributions from Γ_{8c}, Γ_{7c}, and Γ_{6c} need to be removed. The modified parameters are then given by [10,29]

$$\frac{m_0}{m'}=\frac{m_0}{m_e^*}-\frac{2}{3}\frac{E_{P'}}{E_g-E_g'-\Delta_0'}-\frac{1}{3}\frac{E_{P'}}{E_g-E_g'}-\frac{2}{3}\frac{E_P}{E_g}-\frac{1}{3}\frac{E_P}{E_g+\Delta_0},$$

$$g'=g+\frac{2}{3}\frac{E_{P'}}{E_g-E_g'-\Delta_0'}-\frac{2}{3}\frac{E_{P'}}{E_g-E_g'}+\frac{2}{3}\frac{E_P}{E_g}-\frac{2}{3}\frac{E_P}{E_g+\Delta_0},$$

$$\gamma_1'=\gamma_1-\frac{1}{3}\frac{E_{Qr}}{E_g'+\Delta_0'}-\frac{1}{3}\frac{E_{Qr}}{E_g'}-\frac{E_P}{3E_g+\Delta},$$

$$\gamma_2'=\gamma_2+\frac{1}{6}\frac{E_{Qr}}{E_g'}-\frac{E_P}{6E_g+2\Delta},$$

$$\gamma_3'=\gamma_3-\frac{1}{6}\frac{E_{Qr}}{E_g'}-\frac{E_P}{6E_g+2\Delta},$$

$$\kappa'=\kappa-\frac{7}{18}\frac{E_{Qr}}{E_g'+\Delta_0'}+\frac{5}{9}\frac{E_{Qr}}{E_g'}-\frac{E_P}{6E_g+2\Delta},$$

$$q'=q-\frac{2}{9}\frac{E_{Qr}}{E_g'}+\frac{2}{9}\frac{E_{Qr}}{E_g'+\Delta_0'},$$

where $E_P=2m_0P^2/\hbar^2$ is the Kane energy, analogously $E_{P'}=2m_0|P'|^2/\hbar^2$ and $E_{Qr}=2m_0Q_r^2/\hbar^2$. In order to avoid spurious solutions related to losing the ellipticity [45], we reduce the values of E_P and Q. In the first case, we use the rescaling relation [46]

$$E_P=\left(\frac{m_0}{m_e^*}-1\right)\frac{E_g(E_g+\Delta_0)}{E_g+2\Delta_0/3}.$$

For the latter, we reduce the parameter $Q\to Q_r$ to 80% of the original value. Due to the inconsistency of the reported values [10,47], following Ref. [32], we take q from the perturbative formula (see Table IV). Although 14-band $\mathbf{k}\cdot\mathbf{p}$ inherently describes the Dresselhaus coupling, in the case of the reduced Q there is a need of compensation via perturbative formulas.

The relevant part of the Hamiltonian is given by [10]

$$H^{(\mathrm{D})}_{6c8v} = i\frac{\sqrt{3}}{2}[T_x(k_y B^+_{8v}k_z + k_z B^+_{8v}k_y) + \mathrm{c.p.}] + \frac{\sqrt{3}}{2}\Big[(T_{xx} - T_{yy})\Big(\frac{2}{3}k_z B^-_{8v}k_z - \frac{1}{3}k_x B^-_{8v}k_x - \frac{1}{3}k_y B^-_{8v}k_y\Big) - T_{zz}(k_x B^-_{8v}k_x - k_y B^-_{8v}k_y)\Big],$$

$$H^{(\mathrm{D})}_{6c7v} = -\frac{i}{2\sqrt{3}}\big[\sigma_x(k_y B_{7v}k_z + k_z B_{7v}k_y) + \mathrm{c.p.}\big],$$

where

$$B^+_{8v} = \frac{1}{2i}P'(Q - Q_\mathrm{r})\Big(\frac{1}{E_g - E'_g - \Delta'_0} - \frac{1}{E'_g + \Delta'_0} + \frac{1}{E_g - E'_g} - \frac{1}{E'_g}\Big),$$

$$B^-_{8v} = \frac{1}{2i}P'(Q - Q_\mathrm{r})\Big(-\frac{1}{E_g - E'_g - \Delta'_0} + \frac{1}{E'_g + \Delta'_0} + \frac{1}{E_g - E'_g} - \frac{1}{E'_g}\Big),$$

$$B_{7v} = \frac{1}{i}P'(Q - Q_\mathrm{r})\Big(\frac{1}{E_g - E'_g - \Delta'_0} - \frac{1}{E'_g + \Delta_0 + \Delta'_0}\Big).$$

For the eight-band $\mathbf{k}\cdot\mathbf{p}$ calculations, we perform the substitution $P' = 0$, $Q_\mathrm{r} = 0$, and $\Delta^- = 0$ which decouples $\Gamma_{8c} + \Gamma_{7c}$ from the $\Gamma_{6c} + \Gamma_{8v} + \Gamma_{7v}$ block. Further reduction by $P = 0$ and $H^{(\mathrm{D})} = 0$ gives the six-band $\mathbf{k}\cdot\mathbf{p}$ Hamiltonian.

The 4×4 matrix which represents the effective model H_p^{eff} can be split into two 2×2 matrices and diagonalized analytically, with the eigenvalues

$$E_1(B_z) = \tfrac{1}{2}\mu_B g_p B_z - \sqrt{\big(W B_z + \tfrac{1}{2}V_{\mathrm{SO}}\big)^2 + (V_\mathrm{a})^2} + \alpha_p B_z^2,$$

$$E_2(B_z) = -\tfrac{1}{2}\mu_B g_p B_z - \sqrt{\big(W B_z - \tfrac{1}{2}V_{\mathrm{SO}}\big)^2 + (V_\mathrm{a})^2} + \alpha_p B_z^2,$$

$$E_3(B_z) = \tfrac{1}{2}\mu_B g_p B_z + \sqrt{\big(W B_z - \tfrac{1}{2}V_{\mathrm{SO}}\big)^2 + (V_\mathrm{a})^2} + \alpha_p B_z^2,$$

$$E_4(B_z) = -\tfrac{1}{2}\mu_B g_p B_z + \sqrt{\big(W B_z + \tfrac{1}{2}V_{\mathrm{SO}}\big)^2 + (V_\mathrm{a})^2} + \alpha_p B_z^2.$$

[1] D. Loss and D. P. DiVincenzo, Phys. Rev. A **57**, 120 (1998).
[2] P. Recher, E. V. Sukhorukov, and D. Loss, Phys. Rev. Lett. **85**, 1962 (2000).
[3] E. Y. S. Joe, *Spintronics in Nanoscale Devices* (Pan Stanford, Singapore, 2013).
[4] M. Valín-Rodríguez, A. Puente, and L. Serra, Phys. Rev. B **69**, 085306 (2004).
[5] D. V. Bulaev and D. Loss, Phys. Rev. B **71**, 205324 (2005).
[6] A. Manaselyan and T. Chakraborty, Europhys. Lett. **88**, 17003 (2009).
[7] M. Vachon, S. Raymond, A. Babinski, J. Lapointe, Z. Wasilewski, and M. Potemski, Phys. Rev. B **79**, 165427 (2009).
[8] S. Avetisyan, P. Pietiläinen, and T. Chakraborty, Phys. Rev. B **85**, 153301 (2012).
[9] S. Avetisyan, P. Pietiläinen, and T. Chakraborty, Phys. Rev. B **88**, 205310 (2013).
[10] R. Winkler, *Spin-Orbit Coupling Effects in Two-Dimensional Electron and Hole Systems*, Vol. 191 of Springer Tracts in Modern Physics (Springer, Berlin, 2003).
[11] A. L. Efros and M. Rosen, Phys. Rev. B **58**, 7120 (1998).
[12] D. V. Bulaev and D. Loss, Phys. Rev. Lett. **95**, 076805 (2005).
[13] M. V. Durnev, M. M. Glazov, and E. L. Ivchenko, Phys. Rev. B **89**, 075430 (2014).
[14] C. E. Pryor and M. E. Flatté, Phys. Rev. Lett. **96**, 026804 (2006).
[15] G. Medeiros-Ribeiro, M. V. B. Pinheiro, V. L. Pimentel, and E. Marega, Appl. Phys. Lett. **80**, 4229 (2002).
[16] N. A. J. M. Kleemans, J. van Bree, M. Bozkurt, P. J. van Veldhoven, P. A. Nouwens, R. Nötzel, A. Y. Silov, P. M. Koenraad, and M. E. Flatté, Phys. Rev. B **79**, 045311 (2009).
[17] F. Klotz, V. Jovanov, J. Kierig, E. C. Clark, D. Rudolph, D. Heiss, M. Bichler, G. Abstreiter, M. S. Brandt, and J. J. Finley, Appl. Phys. Lett. **96**, 053113 (2010).
[18] A. Schwan, B.-M. Meiners, A. Greilich, D. R. Yakovlev, M. Bayer, A. D. B. Maia, A. A. Quivy, and A. B. Henriques, Appl. Phys. Lett. **99**, 221914 (2011).
[19] T. Nakaoka, T. Saito, J. Tatebayashi, and Y. Arakawa, Phys. Rev. B **70**, 235337 (2004).
[20] T. Andlauer and P. Vogl, Phys. Rev. B **79**, 045307 (2009).
[21] J. van Bree, A. Y. Silov, P. M. Koenraad, M. E. Flatté, and C. E. Pryor, Phys. Rev. B **85**, 165323 (2012).
[22] V. Jovanov, T. Eissfeller, S. Kapfinger, E. C. Clark, F. Klotz, M. Bichler, J. G. Keizer, P. M. Koenraad, M. S. Brandt, G. Abstreiter, and J. J. Finley, Phys. Rev. B **85**, 165433 (2012).
[23] W. Sheng and A. Babinski, Phys. Rev. B **75**, 033316 (2007).
[24] W. Sheng and S. J. Xu, Phys. Rev. B **77**, 113305 (2008).
[25] J. I. Climente, J. Planelles, M. Pi, and F. Malet, Phys. Rev. B **72**, 233305 (2005).
[26] C. Pryor, J. Kim, L. W. Wang, A. J. Williamson, and A. Zunger, J. Appl. Phys. **83**, 2548 (1998).
[27] G. Bester, A. Zunger, X. Wu, and D. Vanderbilt, Phys. Rev. B **74**, 081305 (2006).
[28] M. A. Caro, S. Schulz, and E. P. O'Reilly, Phys. Rev. B **91**, 075203 (2015).
[29] S. Tomić and N. Vukmirović, J. Appl. Phys. **110**, 053710 (2011).
[30] H. Mayer and U. Rössler, Phys. Rev. B **44**, 9048 (1991).
[31] B. A. Foreman, Phys. Rev. B **56**, R12748 (1997).
[32] T. Eissfeller, Ph.D. thesis, Technical University of Munich, 2012.

[33] T. Andlauer, R. Morschl, and P. Vogl, Phys. Rev. B **78**, 075317 (2008).
[34] A. J. Williamson, L. W. Wang, and A. Zunger, Phys. Rev. B **62**, 12963 (2000).
[35] L. He and A. Zunger, Phys. Rev. B **73**, 115324 (2006).
[36] A. Schliwa, M. Winkelnkemper, and D. Bimberg, Phys. Rev. B **76**, 205324 (2007).
[37] M. Zieliński, Phys. Rev. B **86**, 115424 (2012).
[38] J. H. Blokland, F. J. P. Wijnen, P. C. M. Christianen, U. Zeitler, J. C. Maan, P. Kailuweit, D. Reuter, and A. D. Wieck, Phys. Rev. B **75**, 233305 (2007).
[39] P.-L. Ardelt, K. Gawarecki, K. Müller, A. M. Waeber, A. Bechtold, K. Oberhofer, J. M. Daniels, F. Klotz, M. Bichler, T. Kuhn, H. J. Krenner, P. Machnikowski, and J. J. Finley, Phys. Rev. Lett. **116**, 077401 (2016).
[40] A. Mielnik-Pyszczorski, K. Gawarecki, and P. Machnikowski, Sci. Rep. **8**, 2873 (2018).
[41] J. Andrzejewski, G. Sęk, E. O'Reilly, A. Fiore, and J. Misiewicz, J. Appl. Phys. **107**, 073509 (2010).
[42] T. Andlauer, Ph.D. thesis, Technical University of Munich, 2009.
[43] I. Vurgaftman, J. R. Meyer, and L. R. Ram-Mohan, J. Appl. Phys. **89**, 5815 (2001).
[44] V. Mlinar, M. Tadić, B. Partoens, and F. M. Peeters, Phys. Rev. B **71**, 205305 (2005).
[45] G. Yong-Xian, Y. Tao, J. Hai-Ming, X. Peng-Fei, and W. Zhan-Guo, Chinese Phys. B **19**, 088102 (2010).
[46] S. Birner, Ph.D. thesis, Technical University of Munich, 2011.
[47] P. Lawaetz, Phys. Rev. B **4**, 3460 (1971).